

# Prompt Guiding Multi-Scale Adaptive Sparse Representation-driven Network for Low-Dose CT MAR

Baoshun Shi, Bing Chen, Shaolei Zhang, Huazhu Fu, and Zhanli Hu

**Abstract**—Low-dose CT (LDCT) is capable of reducing X-ray radiation exposure, but it will potentially degrade image quality, even yields metal artifacts at the case of metallic implants. For simultaneous LDCT reconstruction and metal artifact reduction (LDMAR), existing deep learning-based efforts face two main limitations: *i*) the network design neglects multi-scale and within-scale information; *ii*) training a distinct model for each dose necessitates significant storage space for multiple doses. To fill these gaps, we propose a prompt guiding multi-scale adaptive sparse representation-driven network, abbreviated as PMSRNet, for LDMAR task. Specifically, we construct PMSRNet inspired from multi-scale sparsifying frames, and it can simultaneously employ within-scale characteristics and cross-scale complementarity owing to an elaborated prompt guiding scale-adaptive threshold generator (PSATG) and a built multi-scale coefficient fusion module (MSFuM). The PSATG can adaptively capture multiple contextual information to generate more faithful thresholds, achieved by fusing features from local, regional, and global levels. Furthermore, we elaborate a model interpretable dual domain LDMAR framework called PDuMSRNet, and train single model with a prompt guiding strategy for multiple dose levels. We build a prompt guiding module, whose input contains dose level, metal mask and input instance, to provide various guiding information, allowing a single model to accommodate various CT dose settings. Extensive experiments at various dose levels demonstrate that the proposed methods outperform the state-of-the-art LDMAR methods.

**Index Terms**—Low-dose computed tomography, Metal artifact reduction, Multi-scale sparse representation, Prompt guiding, Interpretability.

## I. INTRODUCTION

X-ray computed tomography (CT) has been extensively utilized for medical diagnosis. However, the X-ray radiation increases the risk of cancer to patients when aggregated exposure surpasses the specific threshold (Bosch de Basea Gomez et al., 2023). Typically, a reduction in radiation dose is accomplished by managing the electrical current or voltage

This work was supported by the National Natural Science Foundation of China under Grants 62371414 and 61901406, by the Natural Science Foundation of Hebei Province under Grant F2023203043 and F2020203025, by the Young Talent Program of Universities and Colleges in Hebei Province under Grant BJ2021044, and by the Hebei Key Laboratory Project under Grant 202250701010046.

B. S. Shi (Corresponding author), B. Chen, and S. L. Zhang are with the School of Information Science and Engineering, Yanshan University, Qinhuang Dao 066004, China. (E-mail: shibaoshun@ysu.edu.cn).

H. Z. Fu is with the Institute of High Performance Computing, Agency for Science, Technology and Research, 138632, Singapore.

Z. L. Hu is with the Institute of Lauterbur Research Center for Biomedical Imaging, Shenzhen Institute of Advanced Technology, Chinese Academy of Sciences, Shenzhen, 518055, China.

of the X-ray tube. Consequently, low-dose CT (LDCT) is extensively utilized to mitigate X-ray radiation risks. However, the decrease of the X-ray flux level leads to a sinogram (X-ray projection) corrupted by Poisson noise, subsequently yielding the reconstruction corrupted by noise. Additionally, when metallic implants are present within patients, the quality of LDCT images will be further reduced by metal artifacts (Zhou et al., 2022). Therefore, how to simultaneously perform low-dose CT denoising and metal artifact reduction (LDMAR) is a challenge.

With the continuous advancement of deep learning (DL) in medical image processing, various DL-based approaches using deep neural networks (DNNs) have been introduced into the LDCT denoising and full-dose CT (FDCT) MAR. Existing DL-based LDCT denoising or FDCT MAR methods can be primarily categorized into three classes: sinogram domain (Ma et al., 2021; Ghani and Karl, 2020), image domain (Wang et al., 2023a; Liang et al., 2020; Yang et al., 2018; Liao et al., 2020; Li et al., 2023a), and dual domain (Ge et al., 2022; Wu et al., 2023; Wang et al., 2021) methods. Specifically, sinogram domain methods are designed to correct the sinogram and subsequently apply the filtered back-projection (FBP) operation for CT image reconstruction. Image domain methods build DNNs to learn mapping between clean CT images and degraded CT images. In contrast, dual domain methods integrate knowledge from both the sinogram domain and the image domain to construct dual domain networks, achieving significant success. Although aforementioned methods have been developed for LDCT denoising and FDCT MAR tasks, applying previous techniques directly to the LDMAR task produces unsatisfactory reconstructions. To address this issue, [42] first proposed DuDoUFNet, a dual domain under-to-fully-complete progressive restoration network for LDMAR. Nevertheless, DuDoUFNet neglects both multi-scale and within-scale information, limiting its performance, and it also suffers from inadequate model interpretability. In addition, the aforementioned methods suffer from large storage costs at the case of multiple dose levels since they often train each model for the specific setting. This “one-model-for-one setting” approach not only increases storage overhead but also produces inflexible models tailored to single settings, limiting their adaptability in clinical applications. To overcome these bottlenecks, we propose a prompt guiding multi-scale adaptive sparse representation-driven network called PMSRNet which can train a single model for multiple doses, and incorporate it into a dual domain framework to build a model interpretable

network called PDuMSRNet. The main contributions can be summarized as follows:

(1) We come up with a prompt guiding multi-scale adaptive sparse representation-driven network dubbed as PMSRNet. It employs multi-scale sparsifying frames to establish a model-driven multi-scale adaptive network that incorporates both within-scale characteristics and cross-scale complementarity into the overall network. Serving as a plug-and-play module, PMSRNet can be easily generalized to address various image restoration tasks. Specially, we leverage the dose map, metal mask and input instance as prompts, and embedding them into a deep unfolded framework for solving LDMAR task.

(2) We build a prompt guiding scale-adaptive threshold generator (PSATG) capable of adaptively extracting within-scale features for different scales to generate faithful thresholds during the shrinking procedure. The PSATG is composed of a shallow feature extraction module, a deep feature extraction module, a feature selection module, a threshold generating module, and a prompt guiding module. By using a prompt guiding module, the guiding information can be injected into the procedure of generating thresholds under the case of multiple dose levels.

(3) We propose a model interpretable dual domain LDMAR framework. Specifically, we formulate a sparsifying transform-based dual domain optimization model, and solve this optimization problem by using proximal gradient methods. Subsequently, we unfold this iteration algorithm into a deep neural network whose image domain subnetwork is the same architecture as that of PMSRNet, and the sinogram domain subnetwork consists of convolutional residual networks. The comprehensive experiments on the LDMAR task show that the proposed method can produce better results compared to SOTA methods.

## II. RELATED WORK

### A. LDCT Denoising

For LDCT denoising, numerous algorithms have been developed to improve the quality of LDCT images. Traditional methods can be summarized into three main groups, namely sinogram domain filtering (Balda et al., 2012), iterative reconstruction (Lee et al., 2017; Liu et al., 2017), and image post-processing (Chen et al., 2013). The sinogram domain filtering methods employ specific filters to directly suppress noise on raw projection data, potentially causing edge blurring and loss of structural information. The iterative reconstruction methods aim to minimize a unified objective function. However, these methods require raw projection data. In contrast, the image post-processing methods can directly process LDCT images, making them easily integrated into the CT machine system.

Nonetheless, it is challenging for traditional hand-crafted priors to characterize all LDCT images. Recently, DL-based methods show promising reconstruction quality for LDCT denoising due to their powerful image distribution modeling capabilities. Some studies initially developed sinogram domain networks to correct sinograms, followed by using FBP to reconstruct CT images. [8] adopted convolution residual networks to learn mapping between low-dose and full-dose

sinograms. [20] proposed an attention residual dense network address the low-dose sinogram denoising problem. Minor errors in sinograms may introduce new noise and artifacts into the reconstructed images. In contrast, image domain methods directly perform on LDCT images. [4] designed a residual encoder-decoder network to address the LDCT denoising issue. [30] proposed a transformer-based network called CTformer, which incorporates dilated and cyclic shifts to comprehensively capture interactions. [15] proposed an densely connected convolutional neural network with a trainable Sobel convolution design. Since noise stems from the back-projection of corrupted projection data, modeling the noise distribution is challenging. To address the limitation of single domain networks, dual domain methods leverage information from sinogram and image domains for LDCT denoising. [38] proposed a dual domain network based on a 3D residual convolution network. [7] proposed a parallel network to fully and collaboratively utilized dual domain information. [6] proposed an attention-encoding integrated generative adversarial network to achieve efficient full-dose reconstruction. However, these LDCT algorithms do not account for the existence of metallic implants within patients. Therefore, directly applying them for LDMAR may lead to suboptimal reconstruction performance.

### B. FDCT MAR

For FDCT MAR, numerous methods have been proposed and have achieved outstanding performance. Physical effects correction methods model the physical effects of imaging and directly corrects metal-corrupted sinogram regions (Park et al., 2016). However, when high-atomic number metals are present, the metal trace region can be so severely damaged that the above correction methods fail to produce satisfactory results (Zhang and Yu, 2018). Sinogram completion methods utilize various estimation techniques to fill the metal trace region within sinogram (Meyer et al., 2009). As it is difficult to generate perfect estimation, these estimation methods often introduce secondary artifacts. To cope with this problem, iterative reconstruction methods (Chang et al., 2019; Mehranian et al., 2013) are used to reconstruct high-quality CT images from the observed data, but these methods require suitable hand-crafted regularization terms.

With the widespread application of DNNs in medical image processing, numerous DL-based methods have been developed for MAR. [9] employed generative adversarial network to correct metal-corrupted sinogram. Since sinogram domain methods are difficult to produce perfect estimation of the metal trace region, secondary artifacts will inevitably be introduced to the reconstructed image. Image domain methods regard the MAR task as image restoration. [41] utilized DNNs to generate the prior image that assists in correcting the metal-corrupted regions of the sinogram. [16] introduced an unsupervised artifact disentanglement network that produces artifact-reduced images using unpaired training data. The primary limitation of image domain methods is the neglect of the consistency constraint. To address the issue of single domain networks, dual domain methods that exploit dual domain knowledge

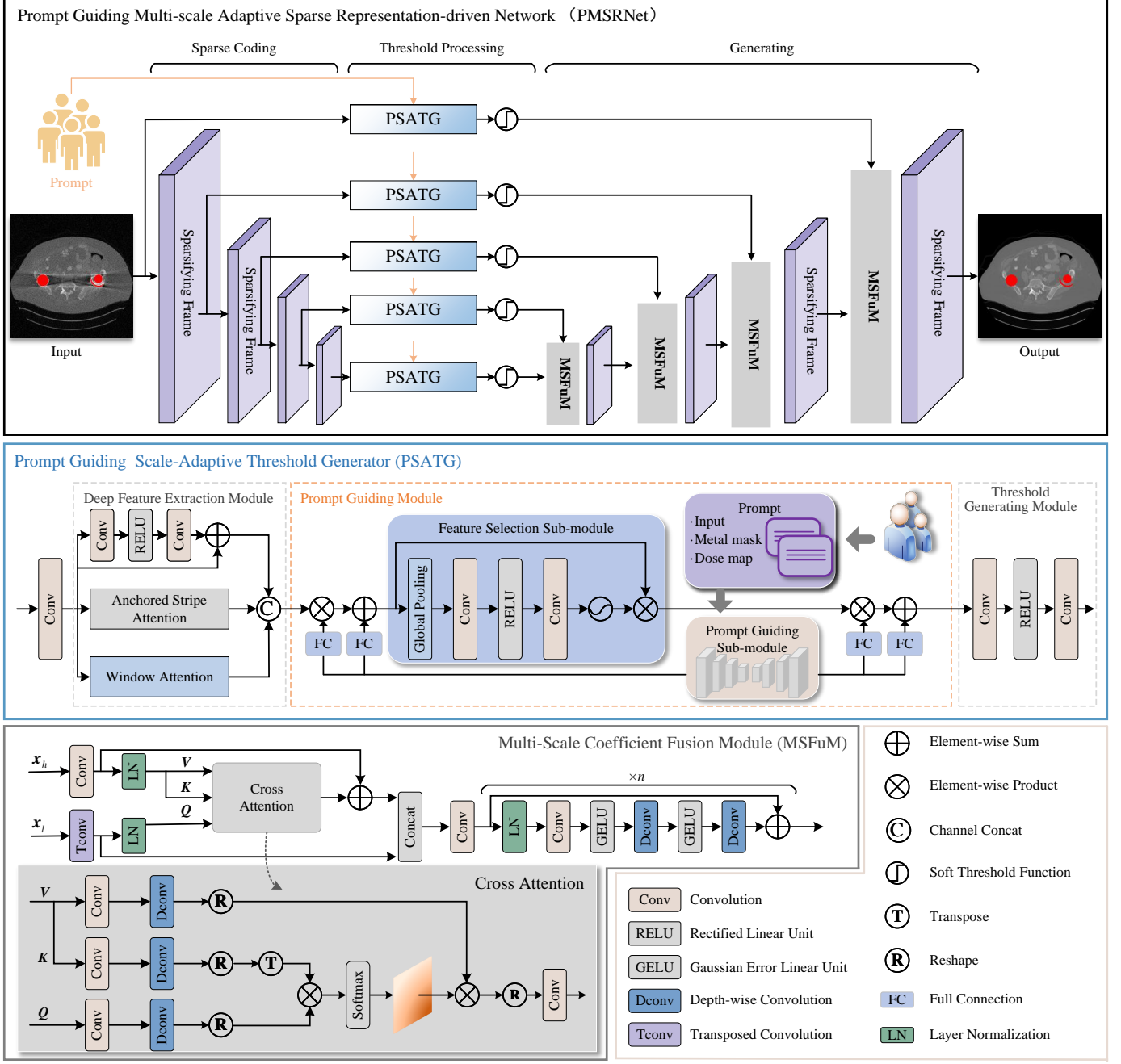


Fig. 1. Overview of our prompt guiding multi-scale adaptive sparse representation-driven network named PMSRNet (top), our prompt guiding scale-adaptive threshold generator termed as PSATG (middle) and multi-scale coefficient fusion module called MSFuM (bottom). The PMSRNet contains three components: multi-scale sparsifying frames, PSATG and MSFuM. The PSATG contains five parts: 1) The shallow feature extraction module relies on a convolution layer; 2) The deep feature extraction module models images at local, regional, and global levels by parallelizing convolutional neural networks, window attention, and anchored stripe attention; 3) The feature selection module utilizes channel attention mechanism to adaptively reweight information from different ranges; 4) The threshold generating module enhances the performance of PMSRNet by generating faithful thresholds using information from the feature selection module; 5) The prompt guiding module utilizes prompt information, including LDCT images with metallic implants, metal masks, and dose maps, to guide the threshold generating process. The MSFuM which is used to fuse low-resolution and high-resolution images mainly contains a cross attention and a feed-forward network.

have been developed these years. The seminal work termed as DuDoNet was proposed by [17], and a Radon inversion layer was designed to bridge between the sinogram domain and the image domain network. [33] proposed a parallel dual domain network by modifying the fixed priority mode of the previous dual domain network. [31] proposed a model-driven dual domain network, integrating imaging geometrical model constraints into the mutual learning process of sinogram and

image domain information. [32] proposed a deep unfolding dual domain network by unfolding the iterative algorithm for MAR task. Although the dual domain network mentioned above have achieved high-quality CT images, the lack of domain knowledge during training remains a significant limitation in improving the MAR performance. [25] proposed a method that leverages sinogram domain, image domain, artifact domain, and coding domain knowledge to construct

a model-driven network for MAR. [29] proposed a novel dual domain network that couples model- and data-driven networks for MAR. Although these networks have achieved excellent performance in MAR tasks, they are designed for full-dose CT and do not address the LDMAR issue. Furthermore, the design of these networks has not considered the incorporation of multi-scale and within-scale information. This leaves room for further improvement.

### III. PROMPT GUIDING MULTI-SCALE ADAPTIVE SPARSE REPRESENTATION-DRIVEN NETWORK

#### A. Architecture Principles

Multi-scale features and cross-scale complementarity are important for solving image inverse problems. [10] proposed MSANet that effectively integrates the within-scale characteristics and cross-scale complementarity for image denoising. Inspired by this, we propose a prompt guiding multi-scale sparse representation-driven network for LDMAR. In PMSRNet, we employ a learnable sparsifying frame to filter the input data for noise removal. More precisely, this process can be expressed as

$$\mathbf{x} = \mathbf{W}^T S_\varepsilon(\mathbf{W}\tilde{\mathbf{x}}) \quad (1)$$

where  $\tilde{\mathbf{x}}$  represents the input LDCT image with metallic implants,  $\mathbf{x}$  represents the filtered CT image,  $\mathbf{W}$  represents the sparsifying frame, and  $S_\varepsilon(\cdot)$  is the soft threshold function defined as  $soft_\varepsilon(\mu) = sign(\mu)max(|\mu| - \varepsilon, 0)$ . To enhance the representation ability of the single-scale sparsifying frame, we extend it to multi-scale sparsifying frames. Specifically, the multi-scale sparsifying frames are sequential structure where information flows between different scales while remaining unchanged within each scale. To obtain multi-scale features, we set the filter sizes in the sparsifying frame network to  $5 \times 5$ ,  $7 \times 7$ ,  $9 \times 9$ , and  $11 \times 11$ , with corresponding output channel numbers of 25, 49, 81, and 121, respectively. The threshold in the soft threshold function plays a crucial role in the sparsifying frame network. Therefore, we construct a prompt guiding scale-adaptive threshold generator to generate faithful thresholds.

As illustrated in Fig. 1, PMSRNet adopts a four-scale architecture consisting of sparse coding procedure, threshold processing procedure, and generating procedure. Specifically, as the number of layers increases, the sparse coding procedure reduces the image resolution by half while also increasing the number of channels to extract features at four different scales. For the threshold processing procedure, the prompt guiding scale-adaptive threshold generator (PSATG) models the features extracted from the sparse coding procedure at local, regional, and global levels to utilize the within-scale characteristics. To attain the desired cross-scale complementarity, the generating procedure involves the fusion of features from high-resolution frame coefficients and low-resolution frame coefficients through a multi-scale coefficient fusion module. In addition, with the decrease in the number of layers, the generating procedure gradually increases the feature resolution while decreasing the number of channels. Next, we introduce the proposed PSATG and MSFuM in detail.

#### B. Prompt Guiding Scale-Adaptive Threshold Generator

Both high-resolution and low-resolution layers require contextual information. When it comes to high-resolution features, reducing their resolution can result in the loss of critical image details. Conversely, if the resolution of low-resolution features is insufficient, it may negatively affect the structural consistency of the reconstructed image. To achieve complementarity of within-scale information, we propose a prompt guiding scale-adaptive threshold generator (PSATG) that can fuse the prompting features and various features from local, regional, and global levels. Specifically, it consists of a shallow feature extraction module, a deep feature extraction module, a feature selection module, a threshold generating module, and a prompt guiding module. The shallow feature extraction module is based on a convolution layer. The deep feature extraction module contains a local information extraction branch (LIEB), a regional information extraction branch (RIEB), and a global information extraction branch (GIEB). LIEB adopts a convolutional residual structure to extract local information. The self-attention branches RIEB and GIEB are built on window attention (Liu et al., 2022) and anchored stripe attention (Li et al., 2023b) to extract regional and global information, respectively. The feature maps are independently processed within three branches and later combined by concatenating them along the channel dimension. The prompt guiding module utilizes prompt information to guide the threshold generating process. More precisely, the initial input feature map undergoes processing through the shallow feature extraction module to generate  $\hat{\mathbf{x}}$ . Next, we perform the three branches on  $\hat{\mathbf{x}}$  to extract local, regional, and global information, respectively. The feature selection module reweights channels corresponding to the three branches, selecting information more conducive to image reconstruction. Finally, the reweighted information is input into the prompt guiding threshold generation module for fusion.

Recently, prompt learning is popular for addressing the all-in-one image restoration (IR) tasks (Potlapalli et al., 2023). This approach not only facilitates generalization across various degradation types and levels, but also consistently achieves SOTA results in IR tasks. However, it often requires various datasets to effectively capture the discriminant features of several IR tasks. For LDMAR task, it is difficult to build various CT datasets. To address this issue, and inspired from prompt learning, we utilize the explicit prompts to guide the threshold generating process. By doing so, the discriminant information for different dose levels can be used to guide the reconstruction network. In this paper, we do not focus on the learning of discriminative information, but rather on improving the overall LDMAR performance. As illustrated in Fig. 1, we take the LDCT images with metallic implants, the metal masks and the dose maps as prompts, and perform a channel-wise concatenation operation on them to obtain the three-channel image  $\mathbf{P}$ . A prompt guiding sub-module represented by  $F_{ext}(\bullet)$  is employed to extract features from the prompt  $\mathbf{P}$ . Subsequently, these features are processed through fully connected layers  $FC(\bullet)$  to achieve the appropriate shape ( $1 \times$  channel or dimension) required for the corresponding

module's outputs. Finally, the output features are multiplied by weight  $\mathbf{k}$  and added by bias  $\mathbf{b}$ . Mathematically, the process of PSATG can be formulated as

$$\mathbf{k}_1 = \text{FC}_1(F_{\text{ext}}(\mathbf{P})), \mathbf{k}_2 = \text{FC}_2(F_{\text{ext}}(\mathbf{P})), \quad (2)$$

$$\mathbf{b}_1 = \text{FC}_3(F_{\text{ext}}(\mathbf{P})), \mathbf{b}_2 = \text{FC}_4(F_{\text{ext}}(\mathbf{P})), \quad (3)$$

$$\mathbf{x}_{\text{in}} = \text{FSM}(\mathbf{k}_1[\text{LIEB}(\mathbf{x}_{\text{in}}), \text{RIEB}(\mathbf{x}_{\text{in}}), \text{GIEB}(\mathbf{x}_{\text{in}})] + \mathbf{b}_1), \quad (4)$$

and

$$\mathbf{x}_{\text{out}} = \text{Conv}(\text{ReLU}(\text{Conv}(\mathbf{k}_2 \mathbf{x}_{\text{in}} + \mathbf{b}_2))) \quad (5)$$

where  $\text{FSM}(\cdot)$  denotes the feature selection module, and  $[\mathbf{x}_1, \mathbf{x}_2, \mathbf{x}_3]$  denotes the channel-wise concatenation of  $\mathbf{x}_1$ ,  $\mathbf{x}_2$ , and  $\mathbf{x}_3$ .

To obtain global range information, we utilize the anchored stripe attention proposed in [14] to model image global range hierarchies. Specifically, we replace the direct comparison of queries and keys with anchors as intermediaries for similarity comparison. Then, we alternate between horizontal and vertical stripes to balance the modeling capacity for global range and the computational complexity.

### C. Multi-Scale Coefficient Fusion Module

High-resolution features possess abundant image details, while low-resolution features contain a wealth of contextual information. To fully leverage cross-scale complementarity, we construct a multi-scale coefficient fusion module (MSFuM) based on the cross attention mechanism, effectively fusing information from multiple scales. The MSFuM within PMSR-Net combines the detailed information from high-resolution features with the contextual information from low-resolution features to obtain complementary multi-scale features across different scales. By doing so, PMSRNet can embrace the complementarity of multi-scale and within-scale information, thereby significantly enhancing the representation ability. As shown in Fig. 1, MSFuM establishes a double-cross attention to fuse high-resolution and low-resolution features. Specifically, we first upsample the low-resolution features  $\mathbf{x}_l$  to match the resolution of the high-resolution features  $\mathbf{x}_h$ , while processing  $\mathbf{x}_h$  with a convolutional layer. Then, the transformed  $\mathbf{x}_l$  and  $\mathbf{x}_h$  are normalized by the LayerNorm. The input  $\mathbf{Q}$  of cross attention originates from  $\mathbf{x}_l$ , while  $\mathbf{K}$  and  $\mathbf{V}$  are obtained from  $\mathbf{x}_h$ . Next, we embed them through convolution and utilize deep convolution to encode channel-wise contextual information. Finally, a reshape operation is utilized to reformulate  $\mathbf{Q}$ ,  $\mathbf{K}$ , and  $\mathbf{V}$  into tokens. Mathematically, this process can be defined as

$$\begin{cases} \tilde{\mathbf{Q}} = \text{R}(\text{Dconv}(\text{Conv}(\mathbf{Q}))) \\ \tilde{\mathbf{K}} = \text{R}(\text{Dconv}(\text{Conv}(\mathbf{K}))) \\ \tilde{\mathbf{V}} = \text{R}(\text{Dconv}(\text{Conv}(\mathbf{V}))) \end{cases} \quad (6)$$

where  $\text{Dconv}$  denotes the depth-wise convolution, and  $\text{R}(\cdot)$  denotes the reshape operation. The softmax function is applied to generate the attention map, which can be expressed as

$$\mathbf{C} = \text{SoftMax}(\tilde{\mathbf{K}}^T \tilde{\mathbf{Q}}). \quad (7)$$

where  $\text{SoftMax}(\bullet)$  is the softmax function applied to re-weight the matrix multiplication. Next, we employ the reshape and convolution operations to further extract features. In summary, cross attention of MSFuM can be expressed as

$$\text{CAttention}(\mathbf{Q}, \mathbf{K}, \mathbf{V}) = \text{Conv}(\text{R}(\tilde{\mathbf{V}} \mathbf{C})). \quad (8)$$

The proposed MSFuM is performed between high-resolution and low-resolution features to extensively explore their correlation, enhancing crucial information and mutually compensating for reconstruction deficiencies.

## IV. THE PROPOSED PMSRNET FOR DUAL DOMAIN LDMAR NETWORK

### A. Model Design and Optimization

Assume that  $\mathbf{x}$  represents the clean CT image, the measurement  $\mathbf{y}$  can be modeled as

$$\mathbf{y} = \mathcal{P}\mathbf{x} + \mathbf{n} \quad (9)$$

where  $\mathcal{P}$  denotes the forward projection (FP) operation under the LDCT condition, and  $\mathbf{n}$  denotes the noise. The linear system in Eqn. (9) is ill-posed, and specific regularization is necessary to address solution ambiguity and suppress noise magnification. A typical optimization model can be expressed as

$$\min_{\mathbf{x}} \|\mathcal{P}\mathbf{x} - \mathbf{y}\|_2^2 + \lambda R(\mathbf{x}) \quad (10)$$

where  $\lambda$  is a regularization parameter, and  $R(\cdot)$  serves as a regularizer to provide prior information about  $\mathbf{x}$ . To facilitate the mutual enhancement of dual domain information, we further perform joint regularization and rewrite Eqn. (10) into

$$\min_{\mathbf{s}, \mathbf{x}} \|\mathcal{P}\mathbf{x} - \mathbf{s}\|_2^2 + \alpha \|\mathbf{s} - \mathbf{y}\|_2^2 + \lambda_1 R_1(\mathbf{s}) + \lambda_2 R_2(\mathbf{x}) \quad (11)$$

where  $\alpha$  is a weight parameter used to balance different data fidelity terms, and  $\mathbf{s}$  is the clean sinogram.  $\lambda_1$  and  $\lambda_2$  are regularization parameters.  $R_1(\cdot)$  and  $R_2(\cdot)$  denote the regularization terms that enforce certain desirable properties onto  $\mathbf{s}$  and  $\mathbf{x}$ , respectively. In fact, sinograms with more uniform profiles are easier to restore (Wang et al., 2021). Therefore, we rewrite  $\mathbf{s}$  as

$$\mathbf{s} = \tilde{\mathbf{y}} \odot \tilde{\mathbf{s}} \quad (12)$$

where  $\odot$  represents the element-wise product, and  $\tilde{\mathbf{y}}$  represents the normalization coefficient, which are typically obtained through a U-Net architecture (Wang et al., 2021). By substituting Eqn. (12) into Eqn. (11), the dual domain LDMAR problem can be formulated as

$$\begin{aligned} \min_{\tilde{\mathbf{s}}, \mathbf{x}} & \|\mathcal{P}\mathbf{x} - \tilde{\mathbf{y}} \odot \tilde{\mathbf{s}}\|_2^2 + \alpha \|\tilde{\mathbf{y}} \odot \tilde{\mathbf{s}} - \mathbf{y}\|_2^2 + \lambda_1 R_1(\tilde{\mathbf{s}}) \\ & + \lambda_2 R_2(\mathbf{x}). \end{aligned} \quad (13)$$

Additionally, we utilize a learnable sparsifying frame to explore the structural information of CT images (Shi and Liu, 2023; Shi et al., 2023; Shi and Lian, 2022). The optimization model can be further expressed as

$$\begin{aligned} \min_{\tilde{\mathbf{s}}, \mathbf{x}} & \|\mathcal{P}\mathbf{x} - \tilde{\mathbf{y}} \odot \tilde{\mathbf{s}}\|_2^2 + \alpha \|\tilde{\mathbf{y}} \odot \tilde{\mathbf{s}} - \mathbf{y}\|_2^2 + \lambda_1 R_1(\tilde{\mathbf{s}}) \\ & + \lambda_2 \|\mathbf{W}\mathbf{x}\|_1 \end{aligned} \quad (14)$$

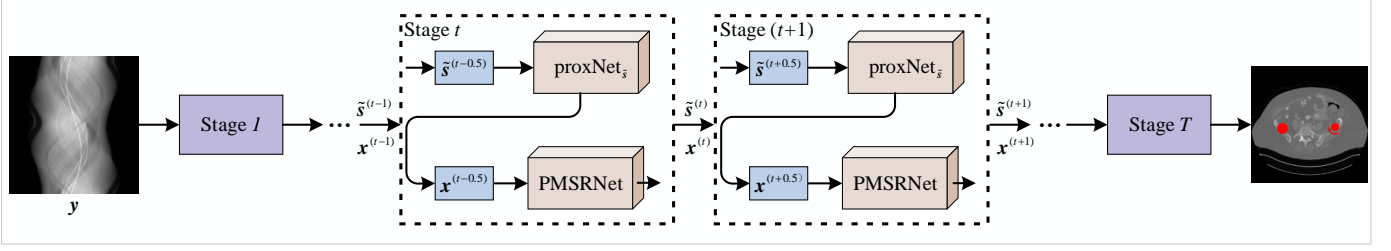


Fig. 2. Overview of our PDuMSRNet with  $T$  stages. At the  $(t+1)$ -th stage,  $\tilde{s}^{(t+1)}$  and  $x^{(t+1)}$  are updated alternately using the  $\text{proxNet}_{\tilde{s}}$  and PMSRNet. Specifically,  $\text{proxNet}_{\tilde{s}}$  comprises three residual blocks, while PMSRNet is the proposed prompt guiding multi-scale adaptive sparse representation-driven network.

where  $\|\cdot\|_1$  represents the  $\ell_1$  norm. To address the optimization problem defined in Eqn. (14), we employ the proximal gradient technique to alternately solve  $\tilde{s}$  and  $x$ . At the  $(t+1)$ -th iteration,  $\tilde{s}$  and  $x$  are solved alternately as follows.

Updating  $\tilde{s}$ : The optimization subproblem for solving  $\tilde{s}$  can be derived as

$$\begin{aligned} \tilde{s}^{(t+1)} = \arg \min_{\tilde{s}} & \left\{ \|\mathcal{P}x^{(t)} - \tilde{y} \odot \tilde{s}\|_2^2 + \alpha \|\tilde{y} \odot \tilde{s} - y\|_2^2 \right. \\ & \left. + \lambda_1 R_1(\tilde{s}) \right\}. \end{aligned} \quad (15)$$

The quadratic approximation with respect to  $\tilde{s}$  in Eqn. (15) can be written as

$$\begin{aligned} \tilde{s}^{(t+1)} = \arg \min_{\tilde{s}} & \left\{ \frac{1}{2} \|\tilde{s} - [\tilde{s}^{(t)} - \eta_1 \bigtriangledown f_1(\tilde{s}^{(t)})]\|_2^2 \right. \\ & \left. + \lambda_1 \eta_1 R_1(\tilde{s}) \right\} \end{aligned} \quad (16)$$

where  $f_1(\tilde{s}^{(t)}) = \|\mathcal{P}x^{(t)} - \tilde{y} \odot \tilde{s}^{(t)}\|_2^2 + \alpha \|\tilde{y} \odot \tilde{s}^{(t)} - y\|_2^2$ , and  $\eta_1$  is the stepsize. Then, the updating rule of  $\tilde{s}$  can be deduced as

$$\tilde{s}^{(t+1)} = \text{prox}_{\lambda_1 \eta_1}(\tilde{s}^{(t+0.5)}) \quad (17)$$

where  $\text{prox}_{\lambda_1 \eta_1}(\cdot)$  is a proximal operator linked to the regularization term  $R_1(\cdot)$  about  $\tilde{s}$ . Based on  $\tilde{s}^{(t+0.5)} = \tilde{s}^{(t)} - \eta_1 \bigtriangledown f_1(\tilde{s}^{(t)})$  and  $\bigtriangledown f_1(\tilde{s}^{(t)}) = \tilde{y} \odot (\tilde{y} \odot \tilde{s}^{(t)} - \mathcal{P}x^{(t)}) + \alpha [\tilde{y} \odot (\tilde{y} \odot \tilde{s}^{(t)} - y)]$ , we have

$$\begin{aligned} \tilde{s}^{(t+0.5)} = & \tilde{s}^{(t)} - \eta_1 [\tilde{y} \odot (\tilde{y} \odot \tilde{s}^{(t)} - \mathcal{P}x^{(t)}) \\ & + \alpha \tilde{y} \odot (\tilde{y} \odot \tilde{s}^{(t)}) - y]. \end{aligned} \quad (18)$$

Updating  $x$ : Similarly, the optimization subproblem for solving  $x$  can be derived as

$$x^{(t+1)} = \arg \min_x \left\{ \|\mathcal{P}x - \tilde{y} \odot \tilde{s}\|_2^2 + \lambda_2 \|\mathbf{W}x\|_1 \right\}. \quad (19)$$

The quadratic approximation with respect to  $x$  in Eqn. (19) can be written as

$$\begin{aligned} x^{(t+1)} = \arg \min_x & \left\{ \frac{1}{2} \|x - [x^{(t)} - \eta_1 \bigtriangledown f_2(x^{(t)})]\|_2^2 \right. \\ & \left. + \lambda_2 \eta_2 \|\mathbf{W}x\|_1 \right\} \end{aligned} \quad (20)$$

where  $\bigtriangledown f_2(x^{(t)}) = \mathcal{P}^T(\mathcal{P}x^{(t)} - \tilde{y} \odot \tilde{s}^{(t+1)})$ , and  $\eta_2$  is the stepsize. The updating rule of  $x$  can be written as

$$x^{(t+1)} = \text{prox}_{\lambda_2 \eta_2}(x^{(t+0.5)}) \quad (21)$$

where  $x^{(t+0.5)} = x^{(t)} - \eta_2 \mathcal{P}^T(\mathcal{P}x^{(t)} - \tilde{y} \odot \tilde{s}^{(t+1)})$ . Eqn. (21) can be approximately solved as

$$x^{(t+1)} = \mathbf{W}^T S_\varepsilon(\mathbf{W}x^{(t+0.5)}) \quad (22)$$

where  $\mathbf{W}$  represents the sparsifying frames.  $S_\varepsilon(\cdot)$  is the soft threshold function. To enhance representation capabilities of the single-scale sparsifying frame, we replace it with the proposed PMSRNet.

### B. Dual Domain Model Interpretable Network

The existing DL-based LDMAR algorithms (Zhou et al., 2022) are data-driven, leading to a lack of model interpretability. However, model interpretability is crucial for building models based on existing knowledge and facilitating subsequent theoretical analysis. How to construct a model interpretable LDMAR network is a challenge. Inspired by the remarkable achievements of deep unfolding techniques in various computer vision tasks, we transform each iterative step in Eqn. (17) and Eqn. (22) into a corresponding network module to build dual domain LDMAR networks, where the network with the prompt guiding module is dubbed as PDuMSRNet, and the network without the prompt guiding module is dubbed as DuMSRNet. Each module of PDuMSRNet corresponds to the implementation operator in the iterative algorithm. In this manner, the proposed PDuMSRNet possesses specific physical interpretability.

As shown in Fig. 2, PDuMSRNet is composed of  $T$  stages, corresponding to  $T$  iterations of the unfolding operations. At each stage, PDuMSRNet consists of a  $\tilde{s}$ -Net and a  $x$ -Net. According to the update rules defined in Eqn. (17) and Eqn. (22), we incrementally construct  $\tilde{s}$ -Net and  $x$ -Net.

**$\tilde{s}$ -Net:** At the  $(t+1)$  stage, given  $\tilde{s}^{(t)}$ ,  $x^{(t)}$ , and  $\tilde{y}$ ,  $\tilde{s}^{(t+0.5)}$  is computed and passed to  $\text{proxNet}_{\tilde{s}}(\cdot)$  to execute the operator  $\text{prox}_{\lambda_1 \eta_1}(\cdot)$ . The  $\text{proxNet}_{\tilde{s}}(\cdot)$  consists of several convolutional residual blocks.

**$x$ -Net:** Similarly, given  $\tilde{s}^{(t+1)}$ ,  $x^{(t)}$ , and  $\tilde{y}$ , the CT image can be updated by the proposed PMSRNet.

### C. Loss Function

During training, we adopt a hybrid dual domain loss function to achieve optimal reconstruction results. First, we adopt mean squared error (MSE) loss function, which can be defined as

$$\mathcal{L}_{mse} = \|\mathbf{m} \odot (\mathbf{x}_{out} - \mathbf{x})\|_2^2 + \omega_1 \|(s_{out} - s)\|_2^2 \quad (23)$$

TABLE I

QUANTITATIVE EVALUATION OF DIFFERENT APPROACHES UNDER 1/2 DOSE, UNDER 1/4 DOSE AND 1/8 DOSE LEVELS. BEST VALUES ARE HIGHLIGHTED IN BOLD. WE REPORT THE PSNR (DB)  $\uparrow$  / SSIM  $\uparrow$  / RMSE (HU)  $\downarrow$  VALUES OF THE TESTING DATASET FOR EACH CASE.

Methods	1/2 Dose			1/4 Dose			1/8 Dose			Average		
	PSNR	SSIM	RMSE									
Single-dose models												
FBP	27.81	0.4455	109.22	26.34	0.3523	127.68	23.99	0.2674	169.49	26.05	0.3551	135.46
LWFSN (Zavala-Mondragon et al., 2022)	34.01	0.7177	53.80	32.83	0.6567	60.80	31.37	0.5973	71.16	32.74	0.6572	61.92
CTformer (Wang et al., 2023a)	37.12	0.9435	39.62	36.57	0.9289	41.56	35.95	0.9241	44.15	36.55	0.9322	41.78
CNN10 (Ghani and Karl, 2018)	37.44	0.9529	38.41	36.94	0.9448	40.32	36.42	0.9387	42.23	36.93	0.9455	40.32
EDCNN (Liang et al., 2020)	37.98	0.9558	35.96	37.54	0.9511	37.46	36.90	0.9447	39.92	37.47	0.9505	37.78
OctaveNet (Won et al., 2020)	38.69	0.9635	32.85	38.12	0.9588	32.85	37.46	0.9521	37.12	38.09	0.9581	34.27
REDCNN (Chen et al., 2017)	38.76	0.9644	32.57	38.28	0.9601	34.07	37.71	0.9544	35.93	38.25	0.9596	34.19
InDuDoNet (Wang et al., 2021)	40.62	0.9651	27.19	40.03	0.9658	28.17	39.44	0.9598	29.78	40.03	0.9636	28.38
DuMSRNet	<b>41.44</b>	<b>0.9750</b>	<b>22.91</b>	<b>40.45</b>	<b>0.9712</b>	<b>26.41</b>	<b>40.06</b>	<b>0.9663</b>	<b>26.24</b>	<b>40.65</b>	<b>0.9708</b>	<b>25.19</b>
Multi-dose models												
BDuMSRNet	41.90	0.9766	22.45	41.18	0.9730	24.06	40.18	0.9674	26.63	41.09	0.9723	24.38
PDuMSRNet	<b>42.26</b>	<b>0.9771</b>	<b>20.76</b>	<b>41.58</b>	<b>0.9742</b>	<b>22.30</b>	<b>40.44</b>	<b>0.9667</b>	<b>25.28</b>	<b>41.43</b>	<b>0.9727</b>	<b>22.78</b>

where  $m$ ,  $x$  and  $s$  represent a binary non-metal mask, the ground truth FDCT image without metallic implants and ground truth full-dose sinogram without metallic implants, respectively.  $\omega_1$  is a weight parameter used to balance different loss components. However, the smooth nature of MSE makes it susceptible to outliers, resulting in the creation of new artifacts. To overcome this problem, consistent with [15] and [13], we adopt the multi-scale perceptual (MSP) loss using a pre-trained ResNet-50 (He et al., 2016), which can be defined as

$$\mathcal{L}_{msp} = \sum_{n=1}^N \|\Psi_n(m \odot x_{out}) - \Psi_n(m \odot x)\|_2^2 \quad (24)$$

where  $\Psi_n(\cdot)$  represents ResNet-50 for the  $n$ -th scale. Finally, the hybrid dual domain loss function can be formulated as

$$\mathcal{L}_{hybrid} = \mathcal{L}_{mse} + \omega_2 \mathcal{L}_{msp} \quad (25)$$

where  $\omega_2$  is a weight parameter used to balance different loss components.

## V. EXPERIMENTS SETTING AND RESULTS

### A. Dataset

Similar to previous MAR work (Yu et al., 2021), we randomly choose 1200 FDCT images from the DeepLesion dataset (Yan et al., 2018). Additionally, the metal masks are obtained from [41], encompassing 100 metal masks of varying location, shape, and size. Subsequently, we select 1000 FDCT images, and synthesize training dataset and validation dataset with 80 and 10 metal masks, respectively. The additional set of 10 metal masks is combined with an additional set of 200 CT images, generating a test dataset of 2000 CT images. The pixel sizes of the selected 10 metal masks for testing are: [2061, 890, 881, 451, 254, 124, 118, 112, 53, 35]. We simply categorize the first four masks as large metals and the latter six as small metals for performance evaluation.

For the selection of simulation parameters and scan geometry, we simulate the equiangular fan-beam projection geometry based on a 120 kVp polyenergetic X-ray source. We introduce Poisson noise to the sinogram to simulate two LDCT scenarios. Specifically, we utilize incident X-ray with  $1 \times 10^5$  photons

to simulate the 1/2 dose level,  $5 \times 10^4$  photons to simulate the 1/4 dose level, and  $2.5 \times 10^4$  photons to simulate the 1/8 dose level. We adjust the size of all images to  $416 \times 416$  pixels and the size of the sinograms to  $641 \times 640$  pixels.

### B. Implementation Details and Evaluation Criteria

During the training of PDuMSRNet, we utilized a total of 3000 images, comprising doses of 1/2, 1/4, and 1/8, with each dose containing 1000 images, to train a universal model. Conversely, during the training of DuMSRNet, we trained three distinct models on images with 1/2, 1/4, and 1/8 dose levels, utilizing 1000 CT images for each dose level. Additionally, to further demonstrate the effectiveness of the prompt guidance strategy, similar to PDuMSRNet, we employed 3000 images to train DuMSRNet and obtain a single model, resulting in a blind DuMSRNet (BDuMSRNet).

We implement our methods using the PyTorch framework, and the differentiable FP and FBP operations are implemented using the ODL library. In our experiments, we manually set  $\alpha = 0.5$ ,  $\eta_1 = 1$ ,  $\eta_2 = 5$ ,  $\omega_1 = 0.01$ , and  $\omega_2 = 1 \times 10^{-4}$ . The total number of epochs is set to 100, with a batch size of 1, utilizing an NVIDIA RTX 4090 GPU. We adopt the Adam optimizer with the parameters  $(\beta_1, \beta_2) = (0.9, 0.999)$  to optimize our network. The initial learning rate is set to  $1 \times 10^{-4}$  and halved at epochs 40 and 80. The peak signal-to-noise ratio (PSNR), structured similarity index measure (SSIM), and root mean square error (RMSE) are employed for quantitatively evaluating the reconstruction outcomes.

### C. Performance Evaluation for LDCT Task

To demonstrate the superiority of DuMSRNet, we conduct both quantitative and qualitative comparisons with previous LDCT methods, such as LWFSN (Zavala-Mondragon et al., 2022), CNN10 (Ghani and Karl, 2018), REDCNN (Chen et al., 2017), CTformer (Wang et al., 2023a), EDCNN (Liang et al., 2020), OctaveNet (Won et al., 2020) and InDuDoNet (Wang et al., 2021), under different dose levels. All methods are trained and tested on the same dataset. Table I summarizes the quantitative results of different methods. It is evident that

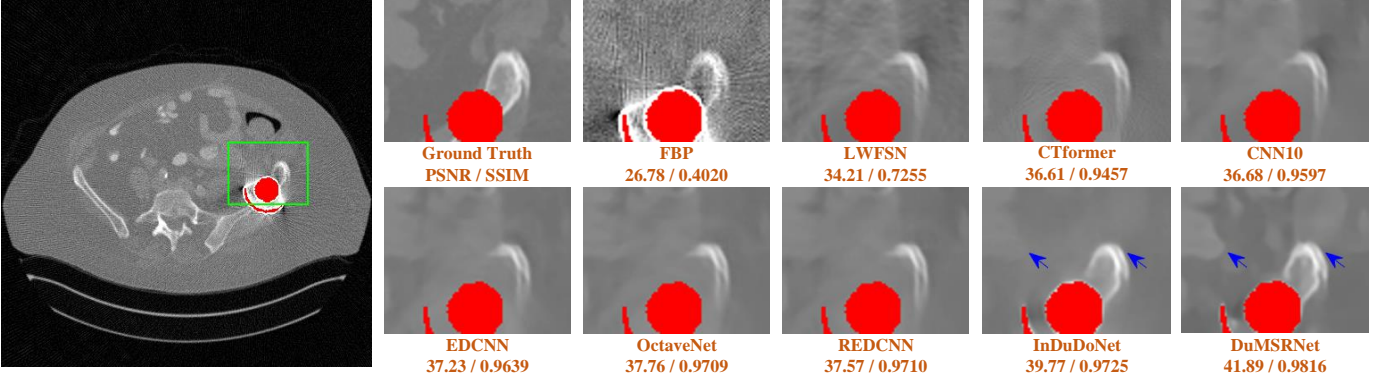


Fig. 3. Visual evaluation of different approaches on LDCT images with metallic implants under the 1/2 dose level. Zooming in on the green screen enhances the viewing experience of the images. The PSNR and SSIM values are computed on the entire image reconstructed by the respective approaches. The metallic implants are highlighted with red masks. The blue arrow indicates the reconstructed structural information. The display window is [-1000, 1000] HU.

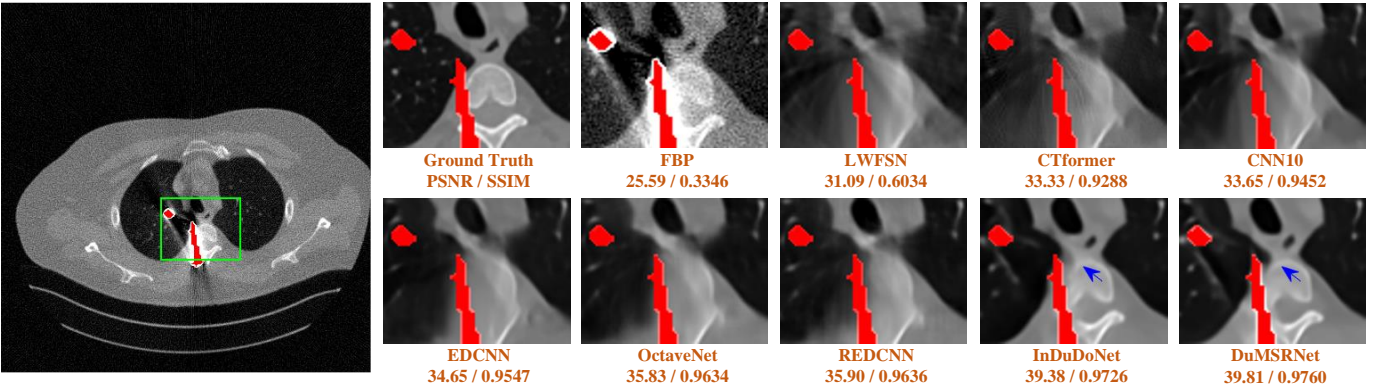


Fig. 4. Visual evaluation of different approaches on LDCT images with metallic implants under the 1/4 dose level. Zooming in on the green screen enhances the viewing experience of the images. The PSNR and SSIM values are computed on the entire image reconstructed by the respective approaches. The metallic implants are highlighted with red masks. The blue arrow indicates the reconstructed structural information. The display window is [-1000, 1000] HU.

DuMSRNet achieves the best performance across all metrics under both dose levels. Fig. 3 illustrates the visual comparison between DuMSRNet and other SOTA methods under the 1/2 dose level. As observed, the FBP reconstructed images are significantly affected by noise and metal artifacts. While LWFSN, CNN10, REDCNN, CTformer, EDCNN, and OctaveNet mitigate certain metal artifacts, they concurrently introduce new noise and metal artifacts. The MAR method InDuDoNet successfully remove most metal artifacts, but they miss tissue details. By contrast, DuMSRNet effectively removes most metal artifacts while preserving the tissue structures in CT images, which demonstrates the importance of multi-scale and within-scale information for LDMAR task. Fig. 4 presents the reconstruction results of various methods under the 1/4 dose level. As shown in Fig. 4, even with a further reduction in dose level to 1/4, DuMSRNet can still remove more noise and artifacts, achieving optimal reconstruction performance.

To validate the efficacy of our prompt guiding strategy, we devised two models: the blind DuMSRNet, trained on a dataset comprising three doses without the prompt guiding strategy, and the PDuMSRNet, trained on a dataset with three doses using the prompt guiding strategy. As shown in Table I, we observed a notable improvement of 0.34 dB in PSNR value for the PDuMSRNet compared to that of the Blind DuMSRNet. This substantial enhancement underscores the efficacy of the prompt guiding strategy. Leveraging prompt

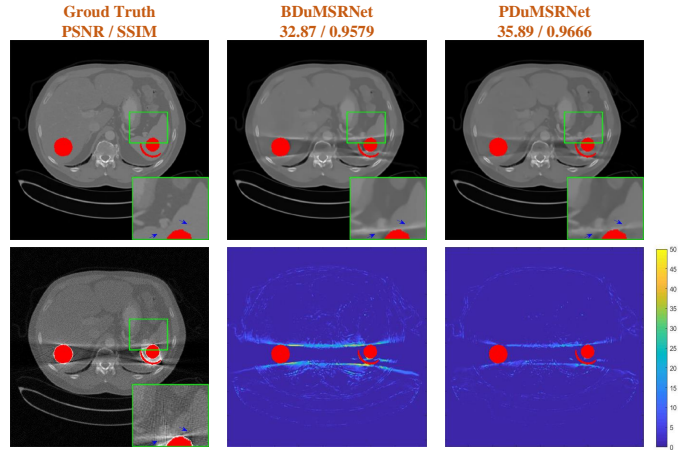


Fig. 5. Visual evaluation and reconstruction error magnitude of BDuMSRNet and PDuMSRNet on LDCT images under the 1/4 dose level. Zooming in on the green screen enhances the viewing experience of the images. The PSNR and SSIM values are computed on the entire image reconstructed by the respective approaches. The metallic implants are highlighted with red masks.

information enables the proposed DuMSRNet to better comprehend the intricate relationship between dose and noise, as well as the nuanced mapping between metal masks and artifacts, thereby achieving superior reconstructions. Fig. 5 illustrates the reconstruction outcomes obtained by BDuMSRNet and PDuMSRNet under the 1/4 dose level. As depicted,

DuMSRNet exhibits superior noise and artifacts removal capabilities compared to BDuMSRNet, resulting in enhanced reconstruction performance. This improvement highlights the effectiveness of the prompt embedding strategy.

TABLE II

STORAGE REQUIREMENT FOR DIFFERENT MODELS. IN COMPARISON REGARDING THE STORAGE COSTS (KB) OF MODELS FOR THREE DOSES, THE MULTIPLE-IN-ONE MODEL DEMONSTRATES BETTER STORAGE EFFICIENCY

Method	Single-dose models		Multi-dose models	
	DuMSRNet	BDuMSRNet	PDuMSRNet	PDuMSRNet
Storage	158,856	52,952	52,996	52,996

#### D. Performance Evaluation on Storage Requirement

To demonstrate the storage efficiency superiority of DuMSRNet, we conduct a qualitative comparison of model storage requirements with the traditional single-dose models (DuMSRNet) and the multi-dose models (BDuMSRNet and PDuMSRNet). As illustrated in Table II, DuMSRNet incurs the highest storage costs among the models. The storage requirement of PDuMSRNet is approximately equivalent to BDuMSRNet, which is one-third that of DuMSRNet. Although the storage cost of the PDuMSRNet is slightly higher than that of the BDuMSRNet, the reconstruction quality achieved by the PDuMSRNet is better than that achieved by the BDuMSRNet.

TABLE III

ABLATION STUDIES OF THE DUAL DOMAIN LEARNING UNDER THE 1/2 DOSE LEVEL. BEST VALUES ARE HIGHLIGHTED IN BOLD.

Network	PSNR (dB) $\uparrow$	SSIM $\uparrow$	RMSE (HU) $\downarrow$
Sinogram-Domain-Only	34.52	0.8545	51.19
Image-Domain-Only	38.30	0.9624	33.78
DuMSRNet	<b>41.44</b>	<b>0.9750</b>	<b>22.91</b>

#### E. Ablation Studies

**(1) The impact of dual domain learning:** During each unfolding stage, DuMSRNet includes a network for the sinogram domain and a network for the image domain. To showcase the effect of dual domain learning, we train sinogram-domain-only and image-domain-only networks under identical conditions. We then compare their performance with DuMSRNet using PSNR, SSIM, and RMSE metrics. As summarized in Table III, it is evident that our dual domain approach (i.e., DuMSRNet) outperforms the sinogram-domain-only and image-domain-only methods, demonstrating the effectiveness of leveraging joint dual domain information.

TABLE IV

ABLATION STUDIES ON DIFFERENT MODULES OF DUMSRNET UNDER THE 1/2 DOSE LEVEL. WE REPORT THE PSNR (dB) / SSIM / RMSE (HU) VALUES OF THE TESTING DATASET FOR EACH CASE. BEST VALUES ARE HIGHLIGHTED IN BOLD.

	Network	PSNR $\uparrow$	SSIM $\uparrow$	RMSE $\downarrow$
DuMSRNet	w/o SATG	40.65	0.9725	22.91
	w/o LIEB	41.09	0.9735	23.89
	w/o RIEB	41.18	0.9736	23.53
	w/o GIEB	40.96	0.9718	24.34
	w/o FEM	41.16	0.9735	23.85
	baseline	<b>41.44</b>	<b>0.9750</b>	<b>22.91</b>

#### (2) The impact of the scale-adaptive threshold generator:

Considering the crucial role of thresholds during the shrinking procedure, we construct a prompt guiding scale-adaptive threshold generator. To validate the effectiveness of prompt guiding scale-adaptive threshold generator (PSATG), we designed two groups of experiments. The first group involves DuMSRNet models at a specific dose of 1/2 to validate the effectiveness of the scale-adaptive threshold generator.

we employ a learnable parameter as the threshold, replacing the threshold generated by SATG, forming DuMSRNet w/o SATG. Note that SATG here does not contain the prompt guiding module. When combined with DuMSRNet and DuMSRNet w/o SATG, the proposed SATG produces a significant performance improvement on all metrics, as summarized in Table IV. To assess the effectiveness of the combination of the deep feature extraction module with three branches and the feature selection module in SATG, we selectively remove the corresponding parts during training, resulting in DuMSRNet w/o LIEB, DuMSRNet w/o RIEB, DuMSRNet w/o GIEB, and DuMSRNet w/o FEM. The corresponding quantitative results are summarized in Table IV. The comparison among DuMSRNet w/o LIEB, DuMSRNet w/o RIEB, DuMSRNet w/o GIEB, and DuMSRNet validates that the combination of local, regional, and global information significantly enhances the reconstruction performance. Additionally, compared to DuMSRNet w/o FEM, DuMSRNet achieves better performance, thanks to the capability of the feature selection module. Specifically, the feature selection module can reweight local, regional, and global information, preventing performance degradation caused by information redundancy.

TABLE V

ABLATION STUDIES ON DIFFERENT PROMPTS OF PDUMSRNET UNDER THE 1/2, 1/4 AND 1/8 DOSE LEVELS. WE REPORT THE PSNR (dB) / SSIM / RMSE (HU) VALUES OF THE TESTING DATASET FOR EACH CASE. BEST VALUES ARE HIGHLIGHTED IN BOLD.

	Prompt	PSNR $\uparrow$	SSIM $\uparrow$	RMSE $\downarrow$
PDuMSRNet	input+mask	34.97	0.9290	69.29
	input+1/dose	35.40	0.9479	61.30
	1/dose+mask	37.88	0.9605	36.50
	input+dose+mask	33.75	0.9280	91.05
	baseline	<b>41.43</b>	<b>0.9727</b>	<b>22.78</b>

**(3) The impact of prompt guiding strategy:** The second group pertains to PDuMSRNet models across multiple dose levels (1/2, 1/4, and 1/8) to validate the effectiveness of the prompt guiding strategy. To facilitate the adaptation of a single model to various CT dose settings, we introduce a prompt guiding strategy that incorporates the prompt information from input LDCT images with metallic implants, mental masks, and dose maps to guide the training process. To evaluate the effectiveness of different prompts, we systematically remove input LDCT images with metallic implants, mental masks, and dose maps, and replace the 1/dose map with the dose map in separate instances. As illustrated in Table V, the performance in these ablation experiments falls short of that of the original PDuMSRNet, thereby confirming the validity of each individual prompt.

**(4) The impact of fusing high-resolution and low-resolution information:** To fully utilize cross-scale comple-

TABLE VI

ABLATION STUDIES ON MSFuM OF DuMSRNet UNDER THE 1/2 DOSE LEVEL. WE REPORT THE PSNR (DB) / SSIM / RMSE (HU) VALUES OF THE TESTING DATASET FOR EACH CASE. BEST VALUES ARE HIGHLIGHTED IN BOLD.

	Network	PSNR ↑	SSIM ↑	RMSE ↓
DuMSRNet	w/o MSFuM	40.55	0.9664	25.19
DuMSRNet	with MSFuM	<b>41.44</b>	<b>0.9750</b>	<b>22.91</b>

mentarity, we design a multi-scale coefficient fusion module using the cross attention mechanism, achieving efficient fusion of multi-scale information. To validate the effectiveness of fusing high-resolution and low-resolution information, we modify the original network architecture to create DuMSRNet w/o MSFuM, where the architecture no longer performs the fusion of high-resolution and low-resolution information. As shown in Table VI, the fusion mechanism of high-resolution and low-resolution leads to an improvement in PSNR values by 0.89 dB, SSIM values by 0.0086, and a reduction in RMSE values by 2.28.

## VI. CONCLUSION

In this paper, we proposed a model interpretable prompt guiding multi-scale adaptive sparse representation-driven network named PMSRNet for LDMAR, and further constructed PDuMSRNet, an enhancement of DuMSRNet in dual domain. Specifically, the PMSRNet consists of three components: multi-scale sparsifying frames, PSATG and MSFuM. The proposed multi-scale sparsifying frames could simultaneously employ within-scale characteristics and cross-scale complementarity. The elaborated PSATG could extract features at the local, regional, and global range to capture multiple contextual information. Additionally, the introduced MSFuM could fuse detailed information from high-resolution features and contextual information from low-resolution features. Extensive experiments demonstrated that the proposed DuMSRNet consistently outperformed the state-of-the-art methods and the proposed PDuMSRNet achieved less model storage cost and more flexibility.

## ACKNOWLEDGMENTS

This work was supported by the National Natural Science Foundation of China under Grants 62371414 and 61901406, by the Natural Science Foundation of Hebei Province under Grant F2023203043 and F2020203025, by the Young Talent Program of Universities and Colleges in Hebei Province under Grant BJ2021044, and by the Hebei Key Laboratory Project under Grant 202250701010046.

## REFERENCES

- [1] Balda, M., Hornegger, J., Heismann, B., 2012. Ray contribution masks for structure adaptive sinogram filtering. *IEEE Transactions on Medical Imaging* 31, 1228–1239. doi:[10.1109/TMI.2012.2187213](https://doi.org/10.1109/TMI.2012.2187213).
- [2] Bosch de Barea Gomez, M., Thierry-Chef, I., Harbron et al., R., 2023. Risk of hematological malignancies from CT radiation exposure in children, adolescents and young adults. *Nature Medicine* 29, 3111–3119. doi:[10.1038/s41591-023-02620-0](https://doi.org/10.1038/s41591-023-02620-0).
- [3] Chang, Z., Ye, D.H., Srivastava, S., Thibault, J.B., Sauer, K., Bouman, C., 2019. Prior-guided metal artifact reduction for iterative X-ray computed tomography. *IEEE Transactions on Medical Imaging* 38, 1532–1542. doi:[10.1109/TMI.2018.2886701](https://doi.org/10.1109/TMI.2018.2886701).
- [4] Chen, H., Zhang, Y., Kalra, M.K., Lin, F., Chen, Y., Liao, P., Zhou, J., Wang, G., 2017. Low-dose CT with a residual encoder-decoder convolutional neural network. *IEEE Transactions on Medical Imaging* 36, 2524–2535. doi:[10.1109/TMI.2017.2715284](https://doi.org/10.1109/TMI.2017.2715284).
- [5] Chen, Y., Yu, F., Luo, L., Toumoulin, C., 2013. Improving abdomen tumor low-dose CT images using dictionary learning based patch processing and unsharp filtering, in: *Proceedings of IEEE Engineering in Medicine and Biology Society (EMBC)*, pp. 4014–4017. doi:[10.1109/EMBC.2013.6610425](https://doi.org/10.1109/EMBC.2013.6610425).
- [6] Fu, Y., Dong, S., Niu, M., Xue, L., Guo, H., Huang, Y., Xu, Y., Yu, T., Shi, K., Yang, Q., Shi, Y., Zhang, H., Tian, M., Zhuo, C., 2023. AIGAN: Attention-encoding integrated generative adversarial network for the reconstruction of low-dose ct and low-dose pet images. *Medical Image Analysis* 86, 102787. URL: <https://www.sciencedirect.com/science/article/pii/S1361841523000488>, doi:<https://doi.org/10.1016/j.media.2023.102787>.
- [7] Ge, R., He, Y., Xia, C., Sun, H., Zhang, Y., Hu, D., Chen, S., Chen, Y., Li, S., Zhang, D., 2022. DDPNet: A novel dual-domain parallel network for low-dose CT reconstruction, in: *Proceedings of the Medical Image Computing and Computer Assisted Intervention (MICCAI)*, pp. 748–757.
- [8] Ghani, M.U., Karl, W., 2018. CNN based sinogram denoising for low-dose CT, in: *Proceedings of Mathematics in Imaging*. doi:[10.1364/MATH.2018.MM2D.5](https://doi.org/10.1364/MATH.2018.MM2D.5).
- [9] Ghani, M.U., Karl, W.C., 2020. Fast enhanced CT metal artifact reduction using data domain deep learning. *IEEE Transactions on Computational Imaging* 6, 181–193. doi:[10.1109/TCI.2019.2937221](https://doi.org/10.1109/TCI.2019.2937221).
- [10] Gou, Y., Hu, P., Lv, J., Zhou, J.T., Peng, X., 2022. Multi-scale adaptive network for single image denoising, in: *Advances in Neural Information Processing Systems*, pp. 14099–14112.
- [11] He, K., Zhang, X., Ren, S., Sun, J., 2016. Deep residual learning for image recognition, in: *Proceedings of IEEE Conference on Computer Vision and Pattern Recognition (CVPR)*, pp. 770–778. doi:[10.1109/CVPR.2016.90](https://doi.org/10.1109/CVPR.2016.90).
- [12] Lee, D., Lee, J., Kim, H., Lee, T., Soh, J., Park, M., Kim, C., Lee, Y.J., Cho, S., 2017. A feasibility study of low-dose single-scan dual-energy cone-beam CT in many-view under-sampling framework. *IEEE Transactions on Medical Imaging* 36, 2578–2587. doi:[10.1109/TMI.2017.2765760](https://doi.org/10.1109/TMI.2017.2765760).
- [13] Li, H., Yang, X., Yang, S., Wang, D., Jeon, G., 2023a. Transformer with double enhancement for low-dose CT denoising. *IEEE Journal of Biomedical and Health In-*

formatics 27, 4660–4671. doi:[10.1109/JBHI.2022.3216887](https://doi.org/10.1109/JBHI.2022.3216887).

[14] Li, Y., Fan, Y., Xiang, X., Demandolx, D., Ranjan, R., Timofte, R., Gool, L.V., 2023b. Efficient and explicit modelling of image hierarchies for image restoration, in: Proceedings of the IEEE/CVF Conference on Computer Vision and Pattern Recognition (CVPR), pp. 18278–18289.

[15] Liang, T., Jin, Y., Li, Y., Wang, T., 2020. EDCNN: Edge enhancement-based densely connected network with compound loss for low-dose CT denoising, in: Proceedings of IEEE International Conference on Signal Processing (ICSP), pp. 193–198. doi:[10.1109/ICSP48669.2020.9320928](https://doi.org/10.1109/ICSP48669.2020.9320928).

[16] Liao, H., Lin, W.A., Zhou, S.K., Luo, J., 2020. ADN: Artifact disentanglement network for unsupervised metal artifact reduction. *IEEE Transactions on Medical Imaging* 39, 634–643. doi:[10.1109/TMI.2019.2933425](https://doi.org/10.1109/TMI.2019.2933425).

[17] Lin, W., Liao, H., Peng, C., Sun, X., Zhang, J., Luo, J., Chellappa, R., Zhou, S.K., 2019. DuDoNet: Dual domain network for CT metal artifact reduction, in: Proceedings of the IEEE/CVF Conference on Computer Vision and Pattern Recognition (CVPR), pp. 10504–10513. doi:[10.1109/CVPR.2019.01076](https://doi.org/10.1109/CVPR.2019.01076).

[18] Liu, L., Li, X., Xiang, K., Wang, J., Tan, S., 2017. Low-dose CBCT reconstruction using hessian schatten penalties. *IEEE Transactions on Medical Imaging* 36, 2588–2599. doi:[10.1109/TMI.2017.2766185](https://doi.org/10.1109/TMI.2017.2766185).

[19] Liu, Z., Hu, H., Lin, Y., Yao, Z., Xie, Z., Wei, Y., Ning, J., Cao, Y., Zhang, Z., Dong, L., Wei, F., Guo, B., 2022. Swin Transformer V2: Scaling up capacity and resolution, in: Proceedings of the IEEE/CVF Conference on Computer Vision and Pattern Recognition (CVPR), pp. 11999–12009. doi:[10.1109/CVPR52688.2022.01170](https://doi.org/10.1109/CVPR52688.2022.01170).

[20] Ma, Y.J., Ren, Y., Feng, P., He, P., Guo, X.D., Wei, B., 2021. Sinogram denoising via attention residual dense convolutional neural network for low-dose computed tomography. *Nuclear Science and Techniques* 32.

[21] Mehranian, A., Ay, M.R., Rahmim, A., Zaidi, H., 2013. X-ray CT metal artifact reduction using wavelet domain  $\ell_0$  sparse regularization. *IEEE Transactions on Medical Imaging* 32, 1707–1722. doi:[10.1109/TMI.2013.2265136](https://doi.org/10.1109/TMI.2013.2265136).

[22] Meyer, E., Bergner, F., Raupach, R., Flohr, T., Kachelrieß, M., 2009. Normalized metal artifact reduction (NMAR) in computed tomography, in: Proceedings of the IEEE Nuclear Science Symposium Conference Record (NSS/MIC), pp. 3251–3255. doi:[10.1109/NSSMIC.2009.5401721](https://doi.org/10.1109/NSSMIC.2009.5401721).

[23] Park, H.S., Hwang, D., Seo, J.K., 2016. Metal artifact reduction for polychromatic X-ray CT based on a beam-hardening corrector. *IEEE Transactions on Medical Imaging* 35, 480–487. doi:[10.1109/TMI.2015.2478905](https://doi.org/10.1109/TMI.2015.2478905).

[24] Potlapalli, V., Zamir, S.W., Khan, S., Khan, F., 2023. PromptIR: Prompting for all-in-one image restoration, in: Proceedings of Conference on Neural Information Processing Systems.

[25] Shi, B., Jiang, K., Zhang, S., Lian, Q., Qin, Y., Zhao, Y., 2024a. Mud-Net: Multi-domain deep unrolling network for simultaneous sparse-view and metal artifact reduction in computed tomography. *Machine Learning: Science and Technology* doi:[10.1088/2632-2153/ad1b8e](https://doi.org/10.1088/2632-2153/ad1b8e).

[26] Shi, B., Lian, Q., 2022. DualPRNet: Deep shrinkage dual frame network for deep unrolled phase retrieval. *IEEE Signal Processing Letters* 29, 1177–1181. doi:[10.1109/LSP.2022.3169695](https://doi.org/10.1109/LSP.2022.3169695).

[27] Shi, B., Liu, K., 2023. Regularization by multiple dual frames for compressed sensing magnetic resonance imaging with convergence analysis. *IEEE/CAA Journal of Automatica Sinica* 10, 2136–2153. doi:[10.1109/JAS.2023.123543](https://doi.org/10.1109/JAS.2023.123543).

[28] Shi, B., Wang, Y., Li, D., 2023. Provable general bounded denoisers for snapshot compressive imaging with convergence guarantee. *IEEE Transactions on Computational Imaging* 9, 55–69. doi:[10.1109/TCI.2023.3241551](https://doi.org/10.1109/TCI.2023.3241551).

[29] Shi, B., Zhang, S., Jiang, K., Lian, Q., 2024b. Coupling model- and data-driven networks for CT metal artifact reduction. *IEEE Transactions on Computational Imaging* 10, 415–428. URL: <https://api.semanticscholar.org/CorpusID:268192663>.

[30] Wang, D., Fan, F., Wu, Z., Liu, R., Wang, F., Yu, H., 2023a. CTformer: convolution-free token2token dilated vision transformer for low-dose CT denoising. *Physics in Medicine & Biology* 68, 065012. doi:[10.1088/1361-6560/acc000](https://doi.org/10.1088/1361-6560/acc000).

[31] Wang, H., Li, Y., Zhang, H., Chen, J., Ma, K., Meng, D., Zheng, Y., 2021. InDuDoNet: An interpretable dual domain network for CT metal artifact reduction, in: Proceedings of the Medical Image Computing and Computer Assisted Intervention (MICCAI), pp. 107–118. doi:[10.1007/978-3-030-87231-1\\_11](https://doi.org/10.1007/978-3-030-87231-1_11).

[32] Wang, H., Li, Y., Zhang, H., Meng, D., Zheng, Y., 2023b. InDuDoNet+: A deep unfolding dual domain network for metal artifact reduction in ct images. *Medical Image Analysis* 85, 102729. URL: <https://www.sciencedirect.com/science/article/pii/S1361841522003577>, doi:<https://doi.org/10.1016/j.media.2022.102729>.

[33] Wang, T., Lu, Z., Yang, Z., Xia, W., Hou, M., Sun, H., Liu, Y., Chen, H., Zhou, J., Zhang, Y., 2022. IDOL-Net: An interactive dual-domain parallel network for CT metal artifact reduction. *IEEE Transactions on Radiation and Plasma Medical Sciences* 6, 874–885. doi:[10.1109/TRPMS.2022.3171440](https://doi.org/10.1109/TRPMS.2022.3171440).

[34] Won, D.K., An, S., Park, S.H., Ye, D.H., 2020. Low-dose CT denoising using octave convolution with high and low frequency bands, in: Proceedings of Predictive Intelligence in Medicine, pp. 68–78.

[35] Wu, Z., Zhong, X., Lyv, T., Wang, D., Chen, R., Yan, X., Coatrieux, G., Ji, X., Yu, H., Chen, Y., Mai, X., 2023. Deep dual-domain united guiding learning with global-local transformer-convolution U-Net for LDCT reconstruction. *IEEE Transactions on Instrumentation and Measurement* 72, 1–10. doi:[10.1109/TIM.2023.3750001](https://doi.org/10.1109/TIM.2023.3750001).

tion and Measurement 72, 1–15. doi:[10.1109/TIM.2023.3329200](https://doi.org/10.1109/TIM.2023.3329200).

[36] Yan, K., Wang, X., Lu, L., Zhang, L., Harrison, A.P., Bagheri, M., Summers, R.M., 2018. Deep lesion graphs in the wild: Relationship learning and organization of significant radiology image findings in a diverse large-scale lesion database, in: Proceedings of the IEEE/CVF Conference on Computer Vision and Pattern Recognition (CVPR), pp. 9261–9270. doi:[10.1109/CVPR.2018.00965](https://doi.org/10.1109/CVPR.2018.00965).

[37] Yang, Q., Yan, P., Zhang, Y., Yu, H., Shi, Y., Mou, X., Kalra, M.K., Zhang, Y., Sun, L., Wang, G., 2018. Low-dose CT image denoising using a generative adversarial network with wasserstein distance and perceptual loss. IEEE Transactions on Medical Imaging 37, 1348–1357. doi:[10.1109/TMI.2018.2827462](https://doi.org/10.1109/TMI.2018.2827462).

[38] Yin, X., Zhao, Q., Liu, J., Yang, W., Yang, J., Quan, G., Chen, Y., Shu, H., Luo, L., Coatrieux, J.L., 2019. Domain progressive 3D residual convolution network to improve low-dose CT imaging. IEEE Transactions on Medical Imaging 38, 2903–2913. doi:[10.1109/TMI.2019.2917258](https://doi.org/10.1109/TMI.2019.2917258).

[39] Yu, L., Zhang, Z., Li, X., Xing, L., 2021. Deep sinogram completion with image prior for metal artifact reduction in CT images. IEEE Transactions on Medical Imaging 40, 228–238. doi:[10.1109/TMI.2020.3025064](https://doi.org/10.1109/TMI.2020.3025064).

[40] Zavala-Mondragon, L.A., Rongen, P., Bescos, J.O., de With, P.H.N., van der Sommen, F., 2022. Noise reduction in CT using learned wavelet-frame shrinkage networks. IEEE Transactions on Medical Imaging 41, 2048–2066. doi:[10.1109/TMI.2022.3154011](https://doi.org/10.1109/TMI.2022.3154011).

[41] Zhang, Y., Yu, H., 2018. Convolutional neural network based metal artifact reduction in X-ray computed tomography. IEEE Transactions on Medical Imaging 37, 1370–1381. doi:[10.1109/TMI.2018.2823083](https://doi.org/10.1109/TMI.2018.2823083).

[42] Zhou, B., Chen, X., Xie, H., Zhou, S.K., Duncan, J.S., Liu, C., 2022. DuDoUFNet: Dual-domain under-to-fully-complete progressive restoration network for simultaneous metal artifact reduction and low-dose ct reconstruction. IEEE Transactions on Medical Imaging 41, 3587–3599. doi:[10.1109/TMI.2022.3189759](https://doi.org/10.1109/TMI.2022.3189759).